Geochemical Perspectives Letters

Silicate and iron phosphate melt immiscibility promotes REE enrichment

S.C. Yan[1,2,3], B. Wan[1*], M. Anenburg[3], J.A. Mavrogenes[3]

OPEN ACCESS

https://doi.org/10.7185/geochemlet.2436

Abstract

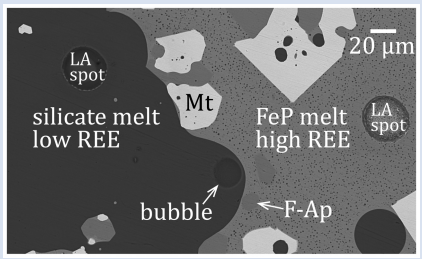

A surging rare earth element (REE) demand calls for finding new REE resources. Iron oxide-apatite (IOA) deposits have substantial REE potential, but their REE enrichment mechanisms remain uncertain, hindering REE exploration. The dominant process of IOA deposit formation is also hotly debated. Here, we use novel layered piston-cylinder experiments to address these questions. Seventeen magmatic FeP–Si immiscibility experiments, across 800–1150 °C, and at 0.4 and 0.8 GPa, reproduced many natural textural (*e.g.*, dendritic magnetite) and geochemical (*e.g.*, $D^{LFeP-LSi}_{Ti/Fe} < 1$) features of IOA deposits. Magmatic-hydrothermal fluid bubbles and iron oxide-bubble pairs formed as well. The results strongly support FeP–Si immiscibility as a controlling factor in IOA deposits, although not mutually exclusive with other models. Light REE partition into FeP liquids, preferentially to heavy REE, explaining the light REE enrichment of IOA deposits. Some $D^{LFeP-LSi}_{REE}$ values reach above 100, much higher than previously reported. Hence, any FeP rich rock that experienced magmatic Fe-Si immiscibility (*e.g.*, IOA, nelsonites) is expected to be light REE enriched and should be considered as a REE exploration target.

Received 1 April 2024 | Accepted 21 August 2024 | Published 24 September 2024

Introduction

Rare earth elements (REEs; lanthanides + Y) are required for modern society to achieve a green energy transition. Iron oxide-apatite (IOA) deposits are globally distributed and formed from the Paleoproterozoic to the Pleistocene (Reich *et al.*, 2022; Yan and Liu, 2022). In IOA deposits, ubiquitous monazite was found in the ~1.88 Ga Kiruna deposit (Pålsson *et al.*, 2014; Yan *et al.*, 2023b), and a significant REE resource (>1 Mt rare earth metals) at Kiruna was recently reported (LKAB, 2023). In addition, iron oxide-phosphate (FeP) tephra containing monazite at the ~2 Ma El Laco deposit (Mungall *et al.*, 2018), REE-rich tailings in ~1.0 Ga deposits in the Adirondacks of New York (Taylor *et al.*, 2019), and a REE-rich breccia pipe containing ~12 wt. % REO at the ~1.4 Ga Pea Ridge deposit (Aleinikoff *et al.*, 2016) further demonstrate that IOA deposits typically contain substantial REE potential (Yan and Liu, 2022).

IOA deposits are related to magmatic rocks (*e.g.*, Troll *et al.*, 2019), yet exactly how they form is unclear. Previous studies suggest the involvement of iron-rich molten salts or hydrosaline liquids (*e.g.*, Bain *et al.*, 2020; Zeng *et al.*, 2024), magnetite-bubble flotation (*e.g.*, Knipping *et al.*, 2015), hydrothermal metasomatic replacement of lava flows (*e.g.*, Sillitoe and Burrows, 2002), with or without magmatic-hydrothermal fluids (*e.g.*, Rojas *et al.*, 2018). In addition, the immiscibility between iron oxide phosphate liquids and silicate magma (FeP–Si) is a commonly invoked process for the formation of IOA deposits (Naslund, 1983; Tornos *et al.*, 2016, 2024; Hou *et al.*, 2018; Keller *et al.*, 2022). However, the exact processes that control the ore-forming processes are hotly debated.

For FeP–Si liquid pairs, experimental studies showed a narrow miscibility gap in dry melts (*i.e.* the compositions of the silicate and FeP melts are closer; Fig. 1a), which widen with lower temperature, higher oxygen fugacity (fO_2), aH_2O, and higher F^- or P_2O_5 contents (*e.g.*, Kamenetsky *et al.*, 2013; Hou *et al.*, 2018). For example, crustal inputs of S^{6+}, F^-, H_2O, Fe and phosphate (*e.g.*, *via* sulfate-evaporites or ironstones) are suggested to widen the Fe–Si immiscibility width in IOA deposits (Lledo *et al.*, 2020; Pietruszka *et al.*, 2023; Tornos *et al.*, 2024). Preliminary work (*e.g.*, Schmidt *et al.*, 2006; Veksler *et al.*, 2006; Lester *et al.*, 2013) indicates that immiscible FeP melts incorporate more REEs than coexisting silicate melts (Fig. 1a). Reliable partition coefficients are only known for narrow immiscibility (nIM, Fig. 1a) conditions. Lester *et al.* (2013) obtained $D^{LFe-LSi}_{REE}$ of ~3–40 at $D^{LFe-LSi}_{SiO_2}$ of ~0.14–0.49 for moderate miscibility gaps (mIM). However, in the Lester *et al.* (2013) phosphate-bearing experiments, lower $D^{LFe-LSi}_{SiO_2}$ values did not always correspond to higher $D^{LFe-LSi}_{REE}$ values (Fig. 1a). For wide miscibility gaps (wIM), Lledo (2005) derived $D^{LFe-LSi}_{Er}$ of 13, but a full set of REE partition coefficients for wide miscibility gaps is still undetermined. The main reasons are (1) few Fe–Si immiscibility experiments contain REEs (Yan and Liu, 2022), and (2) experimentally generated immiscible droplets are typically too small (unless a centrifuge

1. State Key Laboratory of Lithospheric and Environmental Coevolution, Institute of Geology and Geophysics, Chinese Academy of Sciences, Beijing 100029, China
2. College of Earth and Planetary Sciences, University of Chinese Academy of Sciences, Beijing 100049, China
3. Research School of Earth Sciences, The Australian National University, Canberra 2600, Australia
* Corresponding author: (email: wanbo@mail.iggcas.ac.cn)

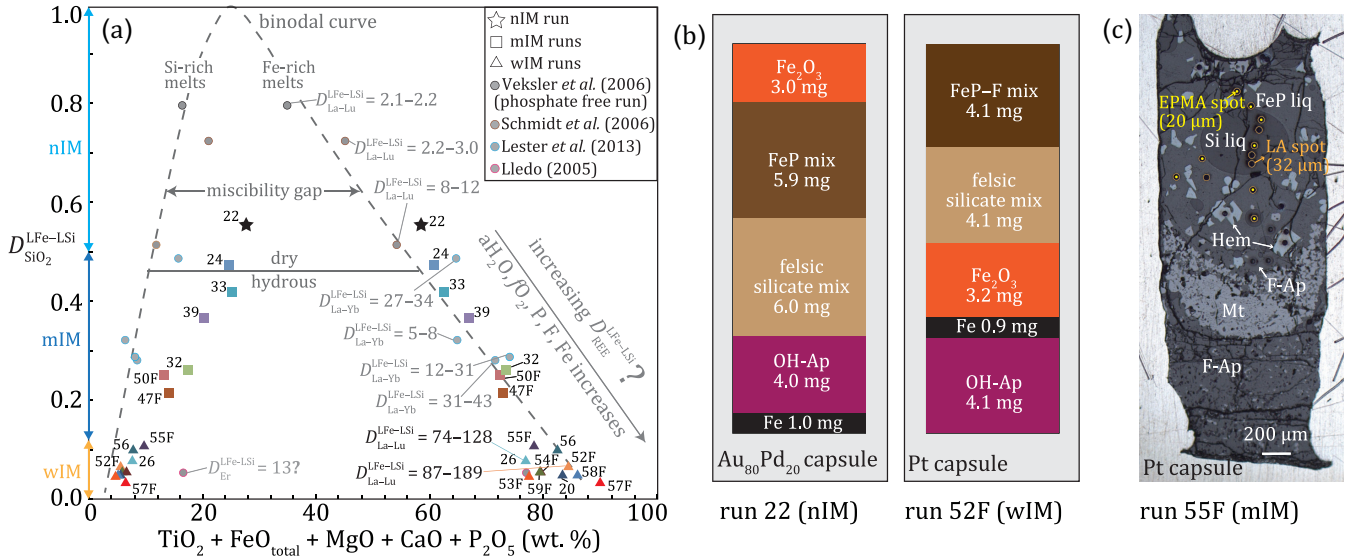

Figure 1 **(a)** Previous immiscibility experiments doped with trace elements, overlain by our new experiments (triangles, squares, and pentagons). Binodal curve and previous dry and hydrous experimental miscibility ranges are from Kamenetsky *et al.* (2013) and Hou *et al.* (2018). The width of the miscibility gap is affected by many variables (*e.g.*, *T*, aH_2O, and others), and this projection captures the combined effect. **(b)** The layered set-up of representative experiments. **(c)** Reflected light image of experiment 55F, with analysis spots for Si and FeP liquids marked. Abbreviations: nIM, $0.5 \leq D^{Fe-LSi}_{SiO_2}$; mIM, $0.12 < D^{Fe-LSi}_{SiO_2} < 0.5$; wIM, $D^{Fe-LSi}_{SiO_2} \leq 0.12$; liq, liquid; F-Ap, fluorapatite; OH-Ap, hydroxyapatite; Mt, magnetite; Hem, hematite.

setup is used), complicating trace element analysis using laser ablation inductively coupled plasma mass spectrometry (LA-ICP-MS) (Schmidt *et al.*, 2006; Veksler *et al.*, 2006).

In this study, we address the origins and REE enrichment mechanisms of IOA deposits *via* a novel piston cylinder layered experimental design (Fig. 1b, c) followed by *in situ* analyses (Fig. 1c).

Methods

We conducted 17 FeP–Si immiscibility experiments over 800–1150 °C for 2–5 days (Fig. 1, Table 1), using a piston cylinder apparatus at the Research School of Earth Sciences, Australian National University (RSES, ANU). Starting materials included felsic silicate mix, FeP, and FeP–F compositions (Table S-1). Water was added in the form of solid hydroxides. These compositions were loaded into noble metal capsules (either Pt or AuPd) together with commercially available hydroxyapatite. Preliminary experiments using homogeneous starting materials resulted in tiny (mostly <5 µm) immiscible liquids. Therefore, subsequent experiments employed layered starting materials to obtain larger immiscible melts for easier geochemical analysis. Natural IOA deposits often contain coexisting hematite and magnetite (Tornos *et al.*, 2024; Xu *et al.*, 2024). Therefore, we aimed to buffer oxygen fugacity at the magnetite–hematite (MH) oxygen buffer by adding layers of $Fe^{3+}{}_2O_3$ and Fe^0 powders, such that some hematite is reduced to magnetite *in situ*. Major and trace elements of immiscible liquids (three to eight points each) were measured using an electron probe microanalyser (EPMA) and laser ablation inductively coupled plasma mass spectrometry (LA-ICP-MS) at the Institute of Geology and Geophysics, Chinese Academy of Sciences (IGGCAS). Analytical spot sizes were typically 20 µm for EPMA and 32 µm for LA-ICP-MS.

Full details of the starting compositions, experimental procedures, geochemical analytical methods, resultant phases, their compositions, and calculated partition coefficients are available in the Supplementary Information.

Assessment of Equilibrium

FeP and silicate liquids were observed in all experiments (Fig. 2). Immiscible liquid droplets were typically well separated (Figs. 1c, 2). Solid crystals were likewise well defined and sized from several to dozens of µm (Figs. 2, S-4). Liquid compositions are shown in Figures 1 and 3 and in the Supplementary Information. Typically, equilibrium between melts is confirmed by reversals, time-series comparisons, or by spatially consistent phase compositions within a single experimental capsule. Previous REE-bearing Fe-Si melt immiscibility experiments containing homogenised starting materials reached equilibrium in less than 1 h at ~1200 °C and 0.2 GPa (Lester *et al.*, 2013). Here, we use spatially consistent compositions as an equilibrium indicator, because manually loaded miniscule powder layers are nearly impossible to consistently reproduce for a constant-composition reversal or time-series experiment. The ratio between the maximum and minimum contents of elements within liquid phase droplets, measured in different places (Figs. 1c, 2b, c, S-6, S-7) within the capsule, is used to show compositional consistency. For example, Table 1 shows this ratio for Ce. The $Ce^{max/min}$ ratio across all FeP liquids ranges from 1.01 to 1.2 and is very close to unity (1.08 ± 0.07, 1 s.d.) considering the measurement uncertainty of 0.01–0.1 (2 s.e.), demonstrating their homogeneous composition. For silicate liquids, the $Ce^{max/min}$ ratios are slightly more variable, presumably because of slower diffusion in the polymerised melt. Nevertheless, excluding the three most variable experiments (53F, 54F, and 59F), the $Ce^{max/min}$ ratio across all silicate liquids is 1.22 ± 0.26 (1 s.d.), again showing homogeneous compositions considering the measurement uncertainty of 0.01–0.3 (2 s.e.). Examples for additional consistent major and trace elements other than Ce are available in the Supplementary Information. The overall consistency of major and trace elements (Table 1, Figs. S-6, S-7), predictable temperature dependence of $D^{FeP-LSi}$ values for wIM and mIM runs (Fig. S-8), and deviation of final liquid elemental contents from starting compositions (Fig. 3) indicate adequate chemical

Table 1 Summary of experimental conditions and products.

No.	Starting layers' mass (mg) FeP, Si, Hem, Fe, OH-Ap	*P* GPa	*T* °C	Duration days	Resultant Phases	Imm. width	Ce of Si liq (max/min)	Ce of FeP liq (max/min)	Equilib-rated?
58F^	4.4(F^), 4.3, 2.7, 1.5, 4.1	0.4	800′	5	**Mt**, F-Ap, whit, Si liq, FeP liq, FeP crystal	wIM	n.a.	n.a.	n.a.
57F	4.4(F), 4.3, 2.5, 1.7, 4.2	0.8	800′	5	**Mt**, F-Ap, Si liq, FeP liq, FeP crystal	wIM	n.a.	n.a.	n.a.
22	5.9, 6.0, 3.0, 1.0, 4.0	0.4	900	5	**Mt**, Si liq, FeP liq	nIM	1.1 ± 0.1[#]	1.18 ± 0.04	Yes
53F	4.0(F), 4.0, 2.7, 1.3, 4.0	0.4	900′	4	**Mt**, **Hem**, F-Ap, q, Si liq, FeP liq, FeP crystal	wIM	5.5 ± 0.3	1.01 ± 0.04	No
26	4.8. 5.1, 3.3, 1, 5.1	0.8	900′	4	**Hem**, whit, Si liq, FeP liq	wIM	1.1 ± 0.1	1.1 ± 0.1	Yes
52F	4.4(F), 4.1, 3.2, 0.9, 4.1	0.8	900′	4	**Mt**, F-Ap, Si liq, FeP liq	wIM	1.3 ± 0.3	1.02 ± 0.08	Yes
20	4.9, 5.1, 3.7, 1.4, 5	0.4	1000′	3	**Mt**, **Hem**, OH-Ap, q, Si liq, FeP liq	wIM	n.a.	n.a.	n.a.
54F	4.3(F), 4.3, 3.3, 1.0, 4.1	0.4	1000′	3	**Hem**, F-Ap, Si liq, FeP liq	wIM	4.1 ± 0.2	1.04 ± 0.02	No
59F	4,2(F), 4.1, 2.6, 1.4, 4.1	0.4	1000′	3	**Mt**, **Hem**, F-Ap, q, Si liq, FeP liq	wIM	2.3 ± 0.2	1.03 ± 0.04	No
55F	4.6(F), 4.6, 3.5, 1.0, 4.5	0.8	1000′	3	**Mt**, **Hem**, F-Ap, Si liq, FeP liq	wIM	1.1 ± 0.1	1.1 ± 0.1	Yes
56	4.2, 4.2, 2.9, 1.2, 4.1	0.8	1000′	3	**Mt**, Whit, OH-Ap, Si liq, FeP liq	wIM	1.9 ± 0.18	1.05 ± 0.03	Yes
47F	4.2(F), 4, 3.2, 1.0, 4.0	0.4	1100′	2	**Mt**, F-Ap, Si liq, FeP liq	mIM	1.5 ± 0.1	1.08 ± 0.05	Yes
24	4.0, 4.0, 3.0, 1.1, 4.0	0.8	1100	4	**Mt**, OH-Ap, Si liq, FeP liq	mIM	1.03 ± 0.05	1.04 ± 0.08	Yes
50F	3.6 (F), 3.2, 2.4, 0.7, 3.2	0.8	1100′	2	**Mt**, F-Ap, Si liq, FeP liq	mIM	1.1 ± 0.1	1.03 ± 0.03	Yes
32	4.4, 5.5, 1.2, 3.5(Mt), 4.9	0.4	1150	3	**Mt**, **Hem**, whit, Si liq, FeP liq	mIM	1.07 ± 0.08	1.2 ± 0.1	Yes
33	4.2, 5.3, 0.8, 4(Mt), 4.7	0.8	1150	3	**Hem**, OH-Ap, Si liq, FeP liq	mIM	1.2 ± 0.1	1.04 ± 0.03	Yes
39	3.7, 5.6, 3.1, 1.5, 4.8	0.8	1150	3	**Mt**, whit, Si liq, FeP liq	mIM	1.05 ± 0.05	1.02 ± 0.03	Yes

Fe-oxide phases as an indicator for fO_2 are marked in bold.
^ 'F' suffix indicates fluoride-bearing experiments by using the FeP–F composition (*e.g.,* 58F, 52F, 50F).
′ Two-step experiments: first heated to 1200 at 150 °C/min and held 20 min for melt homogenisation, then cooled to the target temperature at 40 °C/min (2.5–10 min) and held for 2–5 days.
[#] $Ce^{max/min}$ shown as max/min value ± 2 s.e., with 2 s.e. derived from measurement uncertainty.
Abbreviations: Mt, magnetite; OH-Ap, hydroxyapatite; F-Ap, fluorapatite; Hem, hematite; liq, liquid; whit, whitlockite; q, quartz; wIM, wide immiscibility ($D_{SiO_2}^{LFe-LSi} \leq 0.12$); nIM, narrow immiscibility ($0.5 \leq D_{SiO_2}^{LFe-LSi}$); mIM, moderate immiscibility ($0.12 < D_{SiO_2}^{LFe-LSi} < 0.5$); n.a., not applicable.

exchange and equilibrium between the two liquids, despite the layered experimental design. According to this criterion, immiscible liquids in nIM (22), mIM (24, 33, 39, 32, 50F, 47F) and most of the wIM (52F, 26, 55F, 56) runs reached or were very close (47F, 56) to equilibrium (Table 1). The immiscible liquids of experiments 53F, 54F and 59F showed complex semi-equilibrated conditions using this criterion (Figs. S-9, S-10). Three experiments (20, 57F, 58F) did not contain liquid phases with sufficient size for multiple analyses and were excluded from *D* calculations. However, their textures were informative.

In Fe–Si immiscibility experiments at 0.1 GPa and ~1000 °C by Hou *et al.* (2018)—which excluded REEs and contained homogenised starting materials—immiscible FeP liquids contained µm-scale unidentified droplets (their Figs. 1a, d). We encountered similar textures. Rarely, small inclusions (either crystals or liquid droplets) interfered with EPMA and LA-ICP-MS analyses. For nIM run 22, µm-sized silicate droplets were included within FeP liquids (Fig. 2d). For the mIM runs, FeP liquids contained µm-sized minerals, silicate droplets, and bubbles (Fig. 2g–j). Similarly, for wIM runs, FeP liquids contained µm-sized silicate droplets and bubbles (Fig. 2a–c, e, f). This cross-contamination resulted in some partition coefficients being closer to unity, making the real $D_{REE}^{LFe-LSi}$ values even higher than the already high values we are reporting (Fig. 3d, e). $D_{REE}^{LFe-LSi}$ values of our nIM and mIM runs (Fig. 3d, e) thereby represent lower bound values. For wIM experiments, their low-REE silicate droplets and bubbles were included in a high-REE FeP host, and there is an order of magnitude difference for most element concentrations between the two liquids. Therefore, we consider the contamination-driven effect of lowering $D_{REE}^{LFe-LSi}$ to be negligible for wIM runs. In contrast to the common silicate inclusions within FeP liquids, the opposite was rare. Analysed regions of silicate liquids contained few, if any, FeP liquid droplet impurities (Fig. 2). When present, they were sufficiently large and rare (Fig. 2d, h) to facilitate straightforward analyses of silicate liquid without compromising measurements with spuriously high REE contents.

Five experiments resulted in obvious coexisting magnetite and hematite, and hence their fO_2 is buffered by MH, around 4.5 log units higher than the nickel–nickel oxide (NNO) buffer at our run conditions based on buffer curves determined using the online oxygen fugacity buffer calculator (https://fo2.rses.anu.edu.au/fo2app/, accessed 15 August 2024). Magnetite and hematite were distinguished based on contrasting optical properties in reflected light and Raman spectra (Figs. 1c, S-1). Other single-iron oxide experiments (Table 1) were likely to be close to the MH-buffer since they were prepared in a similar way, such that redox-sensitive elements were still expected to behave as if the runs were MH-buffered. The high oxidation state of the experiments prevented substantial Fe loss to the noble metal capsules, with typical values of ~2 wt. % Fe, and up to a maximum of ~8.4 wt. % Fe, alloyed with capsule materials at the capsule–experiment contact, whereas Fe was below detection limit further away (Fig. S-3).

Chemical Composition of Immiscible Liquids

Elemental systematics in our experiments are consistent with FeP–Si immiscibility during the formation of IOA deposits.

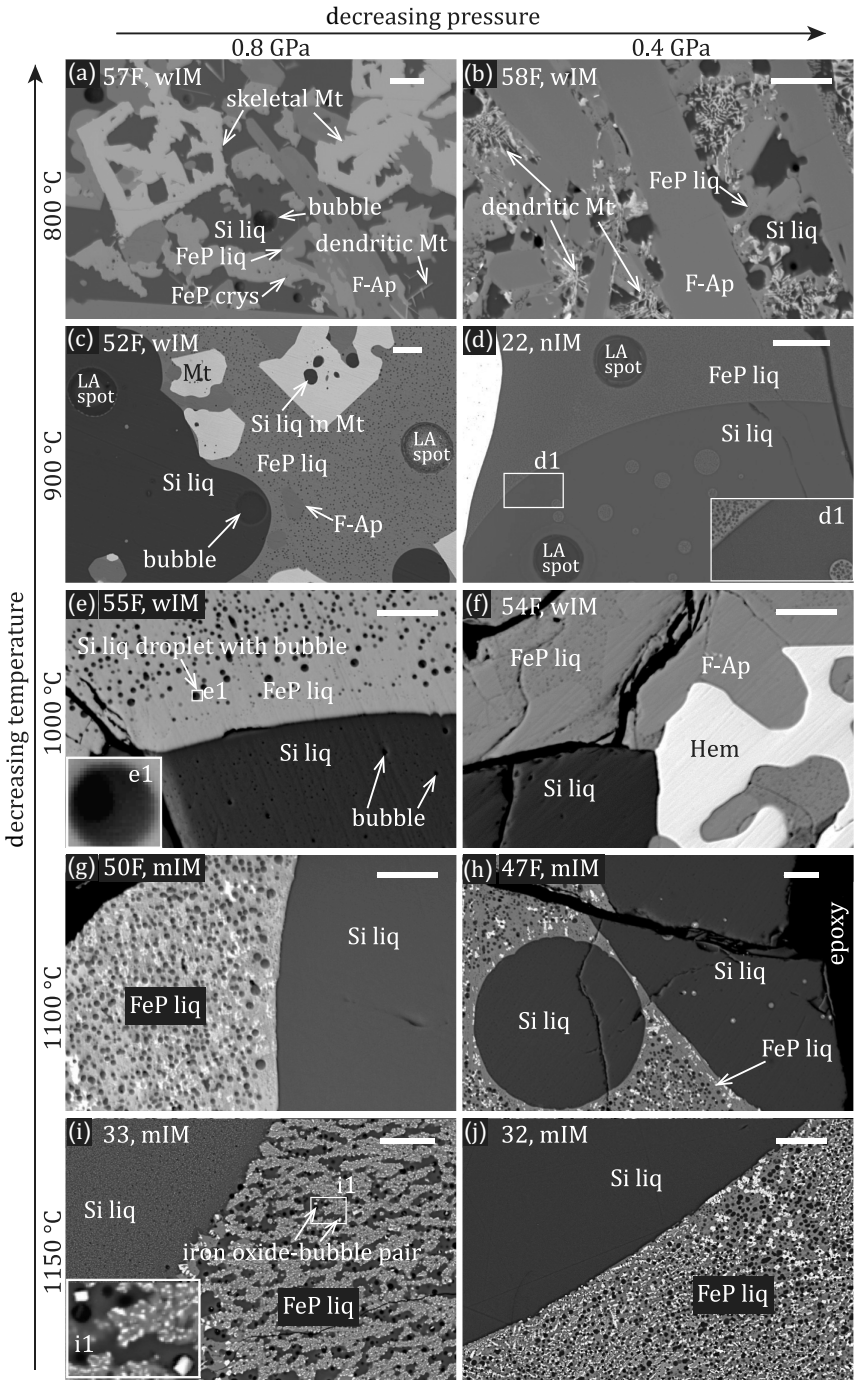

Figure 2 Backscattered images of mineral phases and melt textures from representative experiments. Silicate liquids contain µm-sized Fe-rich droplets at the highest temperatures and pressures (0.8 GPa, 1150 °C; i). FeP liquids contain (or mix with) minerals and silicate liquid droplets, but such contaminants decrease with IM degree, temperature, and pressure (i to c). FeP liquids crystallise substantially between 900 and 800 °C. Scale bar is 20 µm. Abbreviations: liq, liquid; Mt, magnetite; Hem, hematite; F-Ap, fluorapatite; crys, crystal.

We find that $D_{F}^{LFeP-LSi}$, $D_{MgO}^{LFeP-LSi}$, $D_{CaO}^{LFeP-LSi}$, and $D_{P_2O_5}^{LFeP-LSi}$ are all above 1 (Fig. 3, Table S-2), consistent with diopside ($CaMgSi_2O_6$), actinolite [$Ca_2(Mg,Fe)_5(Si_4O_{11})_2(OH)_2$], and fluorapatite [$Ca_5(PO_4)_3F$] as common minerals in IOA deposits. Trace element partition coefficients (Fig. 3) likewise support Th, Co, and V (likely as V^{5+}) enrichment in IOA deposits (Reich *et al.*, 2022; Tornos *et al.*, 2024). Despite $D_{TiO_2}^{LFeP-LSi} > 1$ (Fig. 3), $D_{Ti/Fe}^{LFeP-LSi}$ is below 1 (Fig. 3e), causing Ti/Fe of the FeP liquid to be lower than that of the silicate liquid. Thus, FeP–Si immiscibility dilutes Ti in the FeP liquid relative to Fe, consistent with the typically low Ti contents of IOA magnetite.

FeP–Si Immiscibility Textures

Our experiments show several textural interactions between felsic melt and Fe–Ca–P-rich phases. The experimental temperatures of 800–1150 °C are within the typical homogenisation temperature ranges for melt inclusions in IOA deposits (700–1145 °C; Xie *et al.*, 2019; Bain *et al.*, 2020; Pietruszka *et al.*, 2023; Xu *et al.*, 2024). We observed common silicate liquid droplets in FeP liquids (Fig. 2c, e–j). If such droplets were trapped during magnetite formation (Fig. 2c), then this potentially explains the Si-rich melt inclusions observed in magnetite from the El Laco massive ores (Tornos *et al.*, 2024) and quartz

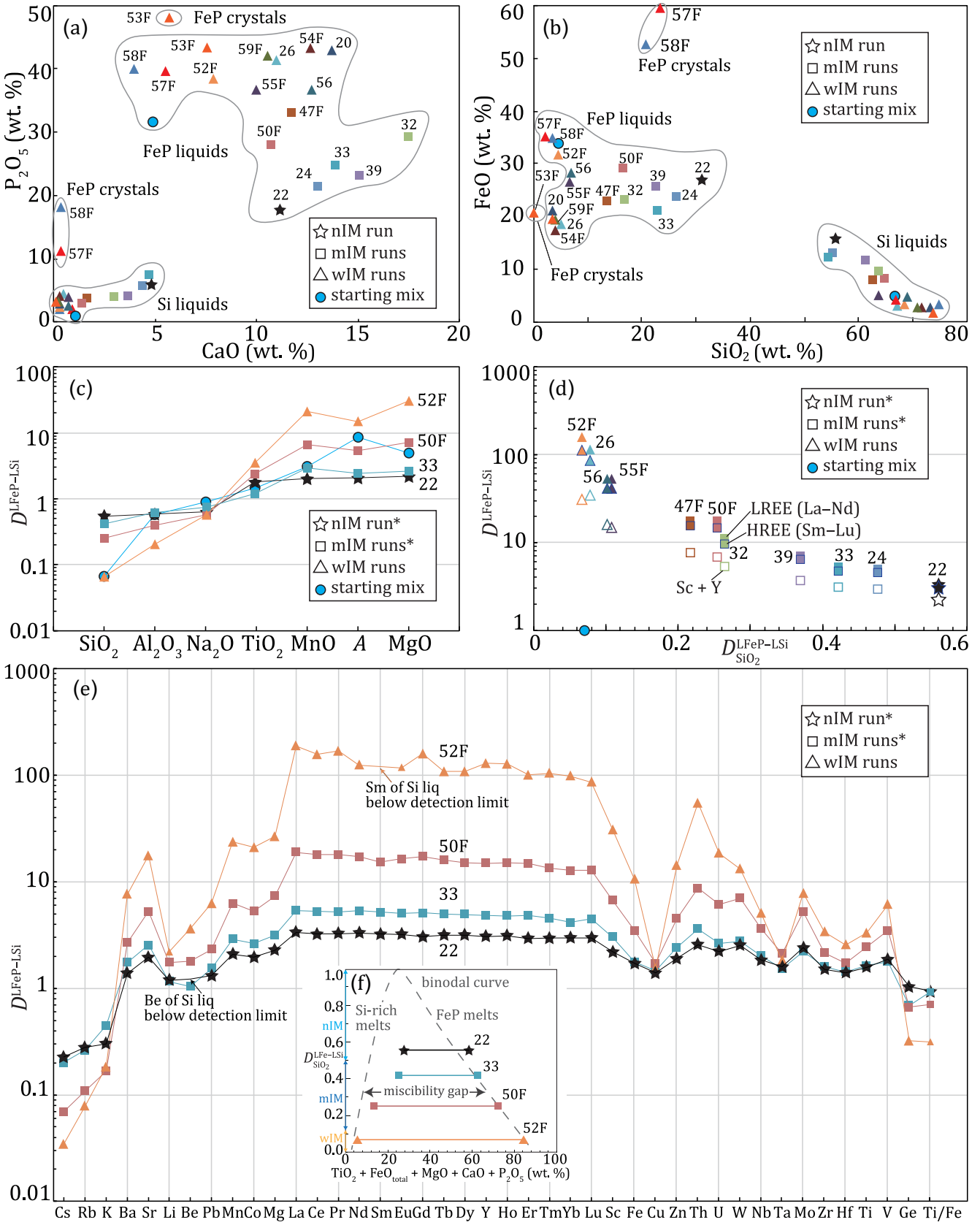

Figure 3 **(a, b)** $CaO–P_2O_5$ and $SiO_2–FeO_t$ plot of two liquids and FeP crystals; **(c)** major element partitioning of representative experiments, $A = TiO_2 + FeO_t + MgO + CaO + P_2O_5$ (wt. %); **(d)** REE partitioning between immiscible melts of 11 runs (Table 1); and **(e)** trace element partitioning between immiscible Si- and FeP-rich melts of representative experiments, with the inset **(f)** showing immiscibility widths. Starting felsic silicate and FeP mix were plotted. *Partition coefficients might be closer to 1 due to impurities in FeP liquids for nIM and mIM runs (Fig. 2), see text for details.

inclusions in earliest-formed magnetite in the El Romel deposit (Rojas *et al.*, 2018). Moreover, imperfect separation of silicate liquid droplets for FeP liquids (Fig. 2) indicates that FeP melts may carry silicate even under wide immiscibility conditions where SiO_2 is nearly insoluble in FeP melts. This may lead to the formation of actinolite, pyroxene, or even quartz, consistent with their occurrence in IOAs (*e.g.*, Nyström and Henríquez, 1994; Mungall *et al.*, 2018; Reich *et al.*, 2022), and particularly in their REE-rich portions (*e.g.*, "Per Geijer" type ore bodies, *e.g.*, Henry, Rektorn and Nukutus, in the Kiruna deposit; Nyström and Henríquez, 1994; LKAB, 2023), which are otherwise expected to be silicate-poor according to wIM equilibrium compositions. FeP liquid droplets surrounded by felsic liquid (Fig. 2d) resemble melt inclusions in feldspar from El Laco (Tornos *et al.*, 2016; Pietruszka *et al.*, 2023).

Skeletal or dendritic magnetite (Fig. 2a, b), generated by rapid quenching of 800 °C runs, remarkably similar to magnetite textures observed in the El Laco and Kiruna IOA deposits (Nyström and Henríquez, 1994), indicating that quenching (and, by implication, probable eruption) of FeP-rich melts occurred during IOA formation. Experiments 53F (0.4 GPa, 900 °C), 57F (0.8 GPa, 800 °C), and 58F (0.4 GPa, 800 °C) yielded FeP liquids and FeP crystals (Figs. 2a, b, 3a, b, S-4), similar to two unidentified FeP phases of El Laco (Xie *et al.*, 2019).

These textural similarities (Fig. S-11) and temperature overlaps suggest our experimental scenarios (narrow to wide FeP–Si immiscibility) may accurately mimic natural processes. The experiments also contain bubbles and iron oxide-bubble pairs indicative of hydrothermal fluid saturation (*e.g.*, Fig. 2c, e, i). Sulfate-evaporite assimilation is hypothesised to be conducive to FeP–Si immiscibility (Pietruszka *et al.*, 2023; Tornos *et al.*, 2024). Iron-bearing hydrosaline liquids, recently proposed to be important for IOA formation (Zeng *et al.*, 2024), were also observed to coexist with immiscible FeP- and Si-rich liquids at El Laco deposit (Pietruszka *et al.*, 2023). Our suggested processes do not preclude—and are in fact compatible with—other proposed processes, such as Fe-rich magmatic hydrothermal fluids (Rojas *et al.*, 2018), iron oxide-bubble pairs (Knipping *et al.*, 2015), Fe-bearing hydrosaline liquids (Zeng *et al.*, 2024), and possibly evaporite assimilation (Pietruszka *et al.*, 2023).

REE Enrichment in IOAs and Fe-REE Associations

Figure 3c–e shows $D^{\mathrm{LFeP-LSi}}$ values of different immiscibility widths, where the gap widens with evolution or cooling (Fig. 1). The general trend is that, with a wider miscibility gap, REE partition more strongly into FeP relative to silicate melts. Our results show that $D^{\mathrm{LFeP-LSi}}_{\mathrm{LREE}}$ and $D^{\mathrm{LFeP-LSi}}_{\mathrm{HREE}}$ can reach above 100 for wide immiscibility (wIM in Fig. 3d, e), so the previously reported $D^{\mathrm{LFeP-LSi}}_{\mathrm{Er}}$ of 13 for wide immiscibility (Lledo, 2005) is unrealistically low. We find that $D^{\mathrm{LFeP-LSi}}_{\mathrm{LREE}}$ values are higher than $D^{\mathrm{LFeP-LSi}}_{\mathrm{HREE}}$, regardless of immiscibility width (Fig. 3d), similar to the findings of Lester *et al.* (2013). The ubiquitous enrichment of LREE relative to HREE in IOA deposits is consistent with this finding and indicates FeP–Si immiscibility is likely a dominant process in IOA deposit formation. Magnetite does not host significant REE; hence, REE in IOA deposits are mainly hosted in phosphates, such as apatite, monazite, and xenotime (Yan and Liu, 2022). Generally, IOA deposits with large iron tonnages and highly evolved portions of IOA deposits (*e.g.*, Pea Ridge, Kiruna, Carmen, and the Fresia deposits) should have higher phosphate contents, and thereby higher REE potential (Yan *et al.*, 2023a).

Other FeP-rich rocks understood to be related to magmatic Fe–Si immiscibility (*e.g.*, nelsonites, Fe-Ti-V deposit such as Panzhihua) experienced a lower immiscibility degree (Lledo *et al.*, 2020) and therefore REE in their Fe-rich parts were less enriched compared to IOA deposits.

Acknowledgements

We appreciate David Clark for aiding piston cylinder experiments, Vivian for Raman analyses, and the support of Microscopy Australia at the CAM, ANU. We also thank Lixin Gu and Dr. Lihui Jia, Jiangyan Yuan, Shitou Wu for helping with geochemical analyses. The work was supported by NSFC 42325206, the Strategy Priority Research Program (Category B) of the CAS (XDB0710000), and ARC Linkage Project LP190100635. Yan appreciates Chinese Scholarship Council (202104910432) for funding the visit to ANU.

Editor: Raul O.C. Fonseca

Additional Information

Supplementary Information accompanies this letter at https://www.geochemicalperspectivesletters.org/article2436.

Cite this letter as: Yan, S.C., Wan, B., Anenburg, M., Mavrogenes, J.A. (2024) Silicate and iron phosphate melt immiscibility promotes REE enrichment. *Geochem. Persp. Let.* 32, 14–20. https://doi.org/10.7185/geochemlet.2436

References

Aleinikoff, J.N., Selby, D., Slack, J.F., Day, W.C., Pillers, R.M., *et al.* (2016) U-Pb, Re-Os, and Ar/Ar geochronology of rare earth element (REE)-rich breccia pipes and associated host rocks from the Mesoproterozoic Pea Ridge Fe-REE-Au deposit, St. Francois Mountains, Missouri. *Economic Geology* 111, 1883–1914. https://doi.org/10.2113/econgeo.111.8.1883

Bain, W.M., Steele-MacInnis, M., Li, K., Li, L., Mazdab, F.K., Marsh, E.E. (2020) A fundamental role of carbonate–sulfate melts in the formation of iron oxide–apatite deposits. *Nature Geoscience* 13, 751–757. https://doi.org/10.1038/s41561-020-0635-9

Hou, T., Charlier, B., Holtz, F., Veksler, I., Zhang, Z., *et al.* (2018) Immiscible hydrous Fe–Ca–P melt and the origin of iron oxide-apatite ore deposits. *Nature Communications* 9, 1415. https://doi.org/10.1038/s41467-018-03761-4

Kamenetsky, V.S., Charlier, B., Zhitova, L., Sharygin, V., Davidson, P., Feig, S. (2013) Magma chamber–scale liquid immiscibility in the Siberian Traps represented by melt pools in native iron. *Geology* 41, 1091–1094. https://doi.org/10.1130/g34638.1

Keller, T., Tornos, F., Hanchar, J.M., Pietruszka, D.K., Soldati, A., *et al.* (2022) Genetic model of the El Laco magnetite-apatite deposits by extrusion of iron-rich melt. *Nature Communications* 13, 6114. https://doi.org/10.1038/s41467-022-33302-z

Knipping, J.L., Bilenker, L.D., Simon, A.C., Reich, M., Barra, F., *et al.* (2015) Giant Kiruna-type deposits form by efficient flotation of magmatic magnetite suspensions. *Geology* 43, 591–594. https://doi.org/10.1130/g36650.1

Lester, G.W., Kyser, T.K., Clark, A.H., Layton-Matthews, D. (2013) Trace element partitioning between immiscible silicate melts with H_2O, P, S, F, and Cl.

Chemical Geology 357, 178–185. https://doi.org/10.1016/j.chemgeo.2013.08.021

LKAB (2023) *Europe's largest deposit of rare earth metals is located in the Kiruna area*. Press release, 12 January 2023, Luossavaara Kiirunavaara AB, Luleå, Sweden. https://mb.cision.com/Main/11419/3696865/1777621.pdf

Lledo, H.L. (2005) *Experimental studies on the origin of iron deposits; and mineralization of Sierra La Bandera, Chile*. Ph.D. thesis, State University of New York at Binghamton.

Lledo, H.L., Naslund, H.R., Jenkins, D.M. (2020) Experiments on phosphate–silicate liquid immiscibility with potential links to iron oxide apatite and nelsonite deposits. *Contributions to Mineralogy and Petrology* 175, 111. https://doi.org/10.1007/s00410-020-01751-8

Mungall, J.E., Long, K., Brenan, J.M., Smythe, D., Naslund, H.R. (2018) Immiscible shoshonitic and Fe-P-oxide melts preserved in unconsolidated tephra at El Laco volcano, Chile. *Geology* 46, 255–258. https://doi.org/10.1130/g39707.1

Naslund, H.R. (1983) The effect of oxygen fugacity on liquid immiscibility in iron-bearing silicate melts. *American Journal of Science* 283, 1034–1059. https://doi.org/10.2475/ajs.283.10.1034

Nyström, J.O., Henríquez, F. (1994) Magmatic features of iron ores of the Kiruna type in Chile and Sweden; ore textures and magnetite geochemistry. *Economic Geology* 89, 820–839. https://doi.org/10.2113/gsecongeo.89.4.820

Pålsson, B.I., Martinsson, O., Wanhainen, C., Fredriksson, A. (2014) Unlocking rare earth elements from European apatite-iron ores. *Proceedings of the 1st European Rare Earth Resources Conference*, 4–7 September 2014, Milos, Greece, 211–220. https://eurare.org/docs/eres2014/fifthSession/BertilPalsson.pdf

Pietruszka, D.K., Hanchar, J.M., Tornos, F., Wirth, R., Graham, N.A., *et al.* (2023) Magmatic immiscibility and the origin of magnetite-(apatite) iron deposits. *Nature Communications* 14, 8424. https://doi.org/10.1038/s41467-023-43655-8

Reich, M., Simon, A.C., Barra, F., Palma, G., Hou, T., Bilenker, L.D. (2022) Formation of iron oxide–apatite deposits. *Nature Reviews Earth & Environment* 3, 758–775. https://doi.org/10.1038/s43017-022-00335-3

Rojas, P.A., Barra, F., Deditius, A., Reich, M., Simon, A., *et al.* (2018) New contributions to the understanding of Kiruna-type iron oxide-apatite deposits revealed by magnetite ore and gangue mineral geochemistry at the El Romeral deposit, Chile. *Ore Geology Reviews* 93, 413–435. https://doi.org/10.1016/j.oregeorev.2018.01.003

Schmidt, M.W., Connolly, J.A.D., Günther, D., Bogaerts, M. (2006) Element partitioning: the role of melt structure and composition. *Science* 312, 1646–1650. https://doi.org/10.1126/science.1126690

Sillitoe, R.H., Burrows, D.R. (2002) New field evidence bearing on the origin of the El Laco magnetite deposit, northern Chile. *Economic Geology* 97, 1101–1109. https://doi.org/10.2113/gsecongeo.97.5.1101

Taylor, R.D., Shah, A.K., Walsh, G.J., Taylor, C.D. (2019) Geochemistry and geophysics of iron oxide-apatite deposits and associated waste piles with implications for potential rare earth element resources from ore and historical mine waste in the eastern Adirondack highlands, New York, USA. *Economic Geology* 114, 1569–1598. https://doi.org/10.5382/econgeo.4689

Tornos, F., Velasco, F., Hanchar, J.M. (2016) Iron-rich melts, magmatic magnetite, and superheated hydrothermal systems: The El Laco deposit, Chile. *Geology* 44, 427–430. https://doi.org/10.1130/g37705.1

Tornos, F., Hanchar, J.M., Steele-MacInnis, M., Crespo, E., Kamenetsky, V.S., Casquet, C. (2024) Formation of magnetite-(apatite) systems by crystallizing ultrabasic iron-rich melts and slag separation. *Mineralium Deposita* 59, 189–225. https://doi.org/10.1007/s00126-023-01203-w

Troll, V.R., Weis, F.A., Jonsson, E., Andersson, U.B., Majidi, S.A., *et al.* (2019) Global Fe-O isotope correlation reveals magmatic origin of Kiruna-type apatite-iron-oxide ores. *Nature Communications* 10, 1712. https://doi.org/10.1038/s41467-019-09244-4

Veksler, I.V., Dorfman, A.M., Danyushevsky, L.V., Jakobsen, J.K., Dingwell, D.B. (2006) Immiscible silicate liquid partition coefficients: implications for crystal-melt element partitioning and basalt petrogenesis. *Contributions to Mineralogy and Petrology* 152, 685–702. https://doi.org/10.1007/s00410-006-0127-y

Xie, Q., Zhang, Z., Hou, T., Cheng, Z., Campos, E., *et al.* (2019) New insights for the formation of kiruna-type iron deposits by immiscible hydrous Fe-P melt and high-temperature hydrothermal processes: evidence from El Laco deposit. *Economic Geology* 114, 35–46. https://doi.org/10.5382/econgeo.2019.4618

Xu, X., Bain, W.M., Tornos, F., Hanchar, J.M., Lamadrid, H.M., *et al.* (2024) Magnetite-apatite ores record widespread involvement of molten salts. *Geology* 52, 417–422. https://doi.org/10.1130/g51887.1

Yan, S., Liu, W. (2022) Rare earth elements in the iron-oxide apatite (IOA) deposit: insights from apatite. *International Geology Review* 64, 3230–3247. https://doi.org/10.1080/00206814.2022.2028198

Yan, S., Wan, B., Andersson, U.B. (2023a) Apatite age and composition: A key to the geological history of the Malmberget Iron-Oxide-Apatite (IOA) deposit and the region. *Journal of Geochemical Exploration* 252, 107267. https://doi.org/10.1016/j.gexplo.2023.107267

Yan, S., Wan, B., Andersson, U.B. (2023b) Hydrothermal circulation at 1.8 Ga in the Kiruna area, northern Sweden, as revealed by apatite geochemical systematics. *Precambrian Research* 395, 107151. https://doi.org/10.1016/j.precamres.2023.107151

Zeng, L.-P., Zhao, X.-F., Spandler, C., Mavrogenes, J.A., Mernagh, T.P., *et al.* (2024) The role of iron-rich hydrosaline liquids in the formation of Kiruna-type iron oxide–apatite deposits. *Science Advances* 10, eadk2174. https://doi.org/10.1126/sciadv.adk2174

Geochemical Perspectives Letters

Silicate and iron phosphate melt immiscibility promotes REE enrichment

S.C. Yan, B. Wan, M. Anenburg, J.A. Mavrogenes

Supplementary Information

The Supplementary Information includes:

1. Rationale for Starting Compositions

Most natural immiscible Fe-rich melts contain 15–40 wt. % SiO_2 (Kamenetsky *et al.*, 2013). Fe-Si immiscibility is widely used to explain the formation of planetary metallic cores, iron oxide apatite deposits, Fe-Ti-P rich rocks, nelsonites, volcanic rocks and the Daly Gap, and layered intrusions (Charlier *et al.*, 2011; Veksler & Charlier, 2015; Fischer *et al.*, 2016; Yokoo *et al.*, 2022; Tornos *et al.*, 2024). Fe-Si immiscibility tends to occur in iron-rich systems, and the miscibility gap is widened by higher oxygen fugacity, phosphate, fluoride, water contents, and lower temperatures (Kamenetsky *et al.*, 2013; Lester *et al.*, 2013; Hou *et al.*, 2018; Lledo *et al.*, 2020). Therefore, we aimed for relatively high oxygen fugacity, iron phosphate, and water contents to match wide immiscibility conditions for Si- and FeP-rich melts.

2. Piston Cylinder Experiments

2.1 Preparation of Starting Materials

Powders of felsic silicate, FeP, and FeP-F compositions (FeP liquid + 7.3 CaF_2 wt. %) were synthesised using high-purity chemicals (Table S-1). Precision balance was used to accurately weigh all chemicals. All chemicals except FeO(OH) and $Al(OH)_3$ were mixed in acetone using an agate mortar and pestle. The mixed powder was made into a pellet and fired at 500 °C for 1 hour in a box furnace to remove CO_2 in Na_2CO_3 and K_2CO_3. Finally, the pellet was crushed to powder and mixed with FeO(OH) and $Al(OH)_3$ to add H_2O. The trace elements powder contains ~60 wt. % SiO_2 and 40 wt. % of most other elements of the periodic table in roughly equal proportions.

Table S-1 Chemicals used, and compositions of starting materials. Here, $D^{LFeP–LSi}$ values represent the elemental ratios between starting FeP and felsic silicate mix, which were used for plotting in Figure 3 in the main text.

Starting felsic silicate mix					Starting FeP mix*				
Chemicals (mg)		Oxides (mg)		wt. %	Chemicals (mg)		Oxides (mg)		wt. %	$D^{LFeP–LSi}$
SiO_2	680	SiO_2	680	66.67	SiO_2	46	SiO_2	46	4.51	0.07
TiO_2	10	TiO_2	10	0.98	TiO_2	15	TiO_2	15	1.47	1.5
$Al(OH)_3$#	137.7	Al_2O_3	90	8.82	$Al(OH)_3$#	79.6	Al_2O_3	52	5.09	0.58
Fe_2O_3	50	Fe_2O_3	50	4.90	FeO(OH)#	36.1	Fe_2O_3	346.8	33.97	6.93
MnO	10	MnO	10	0.98	MnO	31	MnO	31	3.04	3.1
MgO	10	MgO	10	0.98	MgO	50	MgO	50	4.90	5.0
$3CaO·P_2O_5$	20.3	CaO	11	1.08	$3CaO·P_2O_5$	92.2	CaO	50	4.90	4.54
$Na_2O·CO_2$'	34.2	Na_2O	20	1.96	$Na_2O·CO_2$'	30.8	Na_2O	18	1.76	0.90
$K_2O·CO_2$'	58.7	K_2O	40	3.92	$K_2O·CO_2$'	13.2	K_2O	9	0.88	0.22
		P_2O_5	9.28	0.91			P_2O5	321.8	31.52	34.65
					$Fe_2O_3·P_2O_5$	594				
CaF_2	2	F	0.97	0.10	CaF_2	10	F	4.9	0.48	5.05
		Ca	1.03	0.10			Ca	5.1	0.50	4.95
		H_2O	47.72	4.68			H_2O	31.2	3.06	0.65
Trace elements	20	Trace elements	20	1.96	Trace elements	20	Trace elements	20	1.96	1.0
V_2O_5	10	V_2O_5	10	0.98	V_2O_5	10	V_2O_5	10	0.98	1.0
Sc_2O_3	10	Sc_2O_3	10	0.98	Sc_2O_3	10	Sc_2O_3	10	0.98	1.0
Sum	1052.9	Sum	1020.0		Sum	1037.8	Sum	1020.8		
		CO_2'	32.9				CO_2'	17.0		

* FeP-F mix = FeP mix + 7.3 CaF_2 wt. %.
# OH^- bearing chemicals added after firing CO_2' at 500 °C for 1 hour in furnace.
' CO_2 was fired, so the final mixes do not contain CO_2.

2.2 High Temperature and Pressure Experiments

To prepare capsules, a noble metal tube was cut and welded on one side. Capsule materials are Pt, except $Au_{80}Pd_{20}$ for run 22, and $Au_{20}Pd_{80}$ for runs 20 and 39. Different layers (Table S-1) were weighed by precision balance and added into the capsule, followed by welding of the other side of the tube. Cylindrical assemblies of 5/8-inch NaCl sleeve, Pyrex, graphite, MgO, and the capsule were put into the piston cylinder apparatus to start the experiment. The temperature was monitored using type B thermocouple. Initial heating rate was 150 °C/min. Experiments were terminated by quenching to room temperature in 10–15 seconds. The capsules were then removed from the assembly and mounted in epoxy for polishing and further observations and geochemical analyses.

3. Microscope, EDS and Raman Analyses

Optical microscope and scanning electron microscope (SEM) were used to obtain optical and back-scattered electron (BSE) images and identify the experimental phase assemblages. A Zeiss Gemini450 and Nova NanoSEM 450 at the Institute of Geology and Geophysics, Chinese Academy of Sciences (IGGCAS), and a Hitachi 4300 at the Centre for Advanced Microscopy (CAM), the Australian National University were used, operating at ~15 kV and a beam current of ~1–2 nA. Raman spectroscopy was carried out at RSES, ANU, using a Horiba LabRAM Soleil spectrometer.

Magnetite and hematite were identified under reflected light by their different colour and extinction character in polarised light (*e.g.*, magnetite has complete extinction), as well as their Raman spectra (Fig. S-1). Apatite and whitlockite were identified by energy dispersive spectrometry (EDS) semi-quantifying the relative Ca and P content, as apatite contains more Ca than P, whereas whitlockite contains more P than Ca (Fig. S-2). Microstructures of quenched melts can be observed by high resolution BSE imaging. EDS analyses showed minor Fe absorption of capsules (Fig. S-3). Experimental textures of runs not shown in the main text are given in Figure S-4.

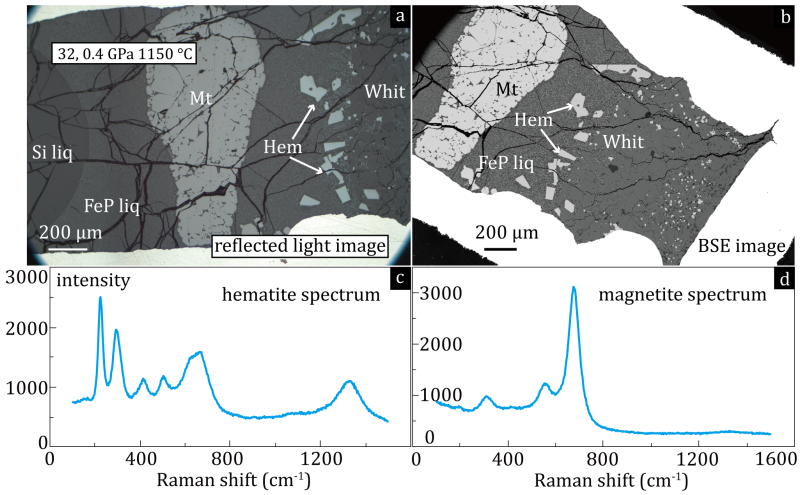

Figure S-1 Identification of magnetite and hematite. Large grains show **(a)** different colours in reflected light, **(b)** almost indistinguishable brightness under BSE image**,** and **(c, d)** distinct Raman spectra. Identification is more difficult for tiny µm-scale grains.

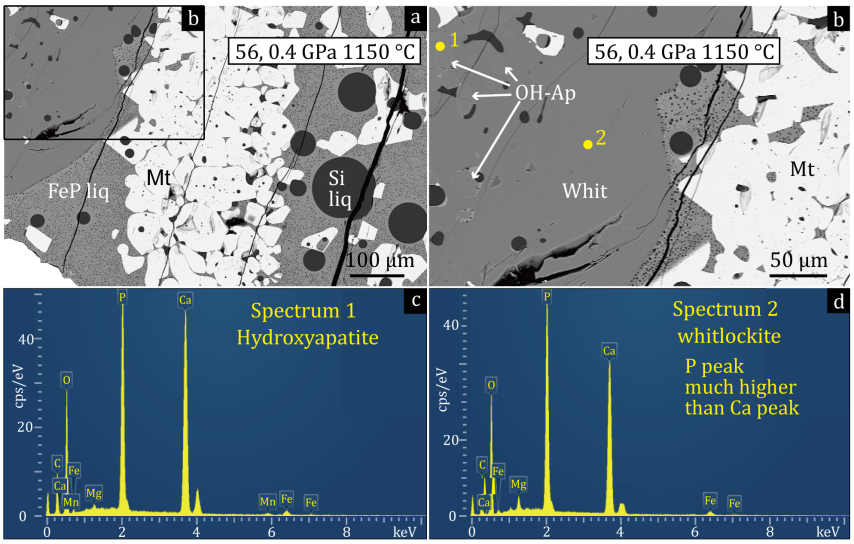

Figure S-2 Identification of apatite and whitlockite by **(a, b)** minor differences in BSE brightness and **(c, d)** contrasting EDS spectra.

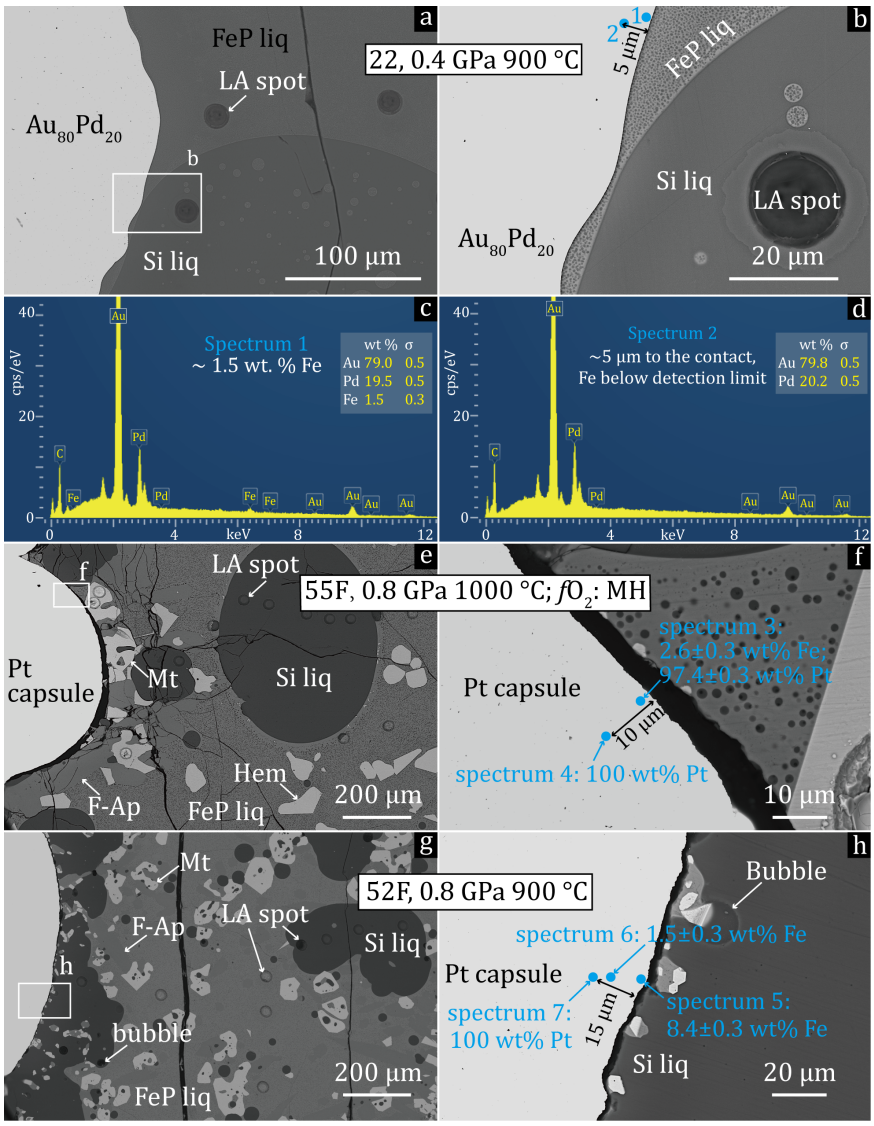

Figure S-3 **(c, d, f, h)** Fe absorption by capsule materials as shown by EDS analyses; panels **(a, b, e, g)** indicate areas of analyses. The most severe case shown in h, where Fe content reaches up to ~8.4 wt. % at the capsule-experiment contact, whereas it is below detection limit at ~15 µm from the contact.

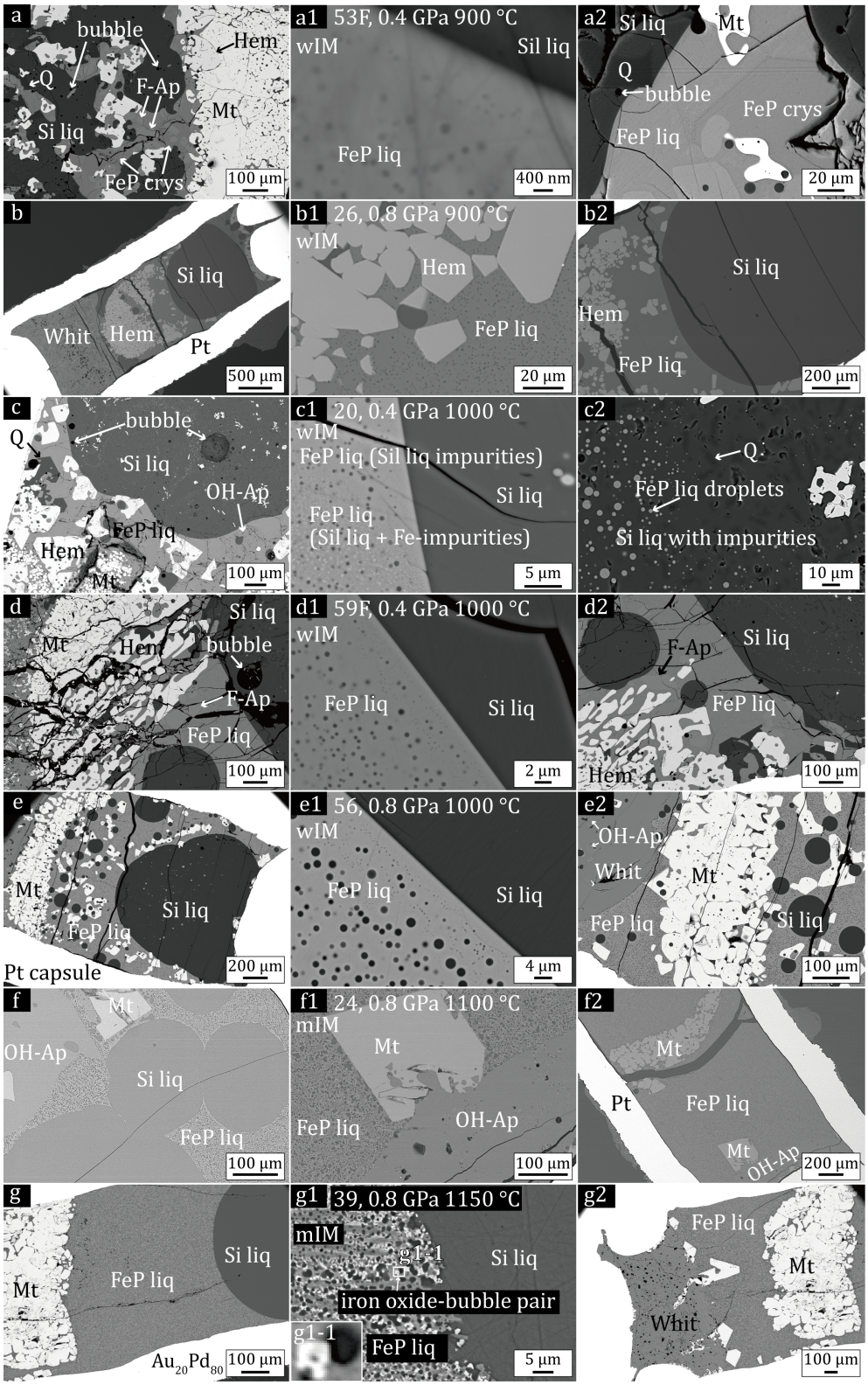

Figure S-4 BSE images of seven runs not shown in main text, with run conditions listed in **(a1-f1)**. Abbreviations: Q, quartz; Hem, Hematite; Mt, magnetite; Si liq, silicate liquid; crys, crystal; F-Ap, fluorapatite; OH-Ap, hydroxyapatite; Whit, whitlockite; Pt, Platinum; nIM, narrow immiscibility; mIM, moderate immiscibility; wIM, wide immiscibility.

4. Major Element Analyses

Major elements of all synthetic immiscible FeP- and Si-rich liquids and FeP crystals were analysed by wavelength-dispersive spectrometry (WDS) on a JEOL JXA-8100 electron probe microanalyser at IGGCAS, with an accelerating voltage of 15 kV and a beam current of 20 nA. Spot size diameters were 20 μm, except for 5 μm in cases of small FeP liquids in runs 57F and 58F. For glasses, three to seven points (Fig. S-5) were measured and presented as average in the main text. Natural minerals and synthetic oxides were used as standards, and the ZAF procedure was used for matrix corrections.

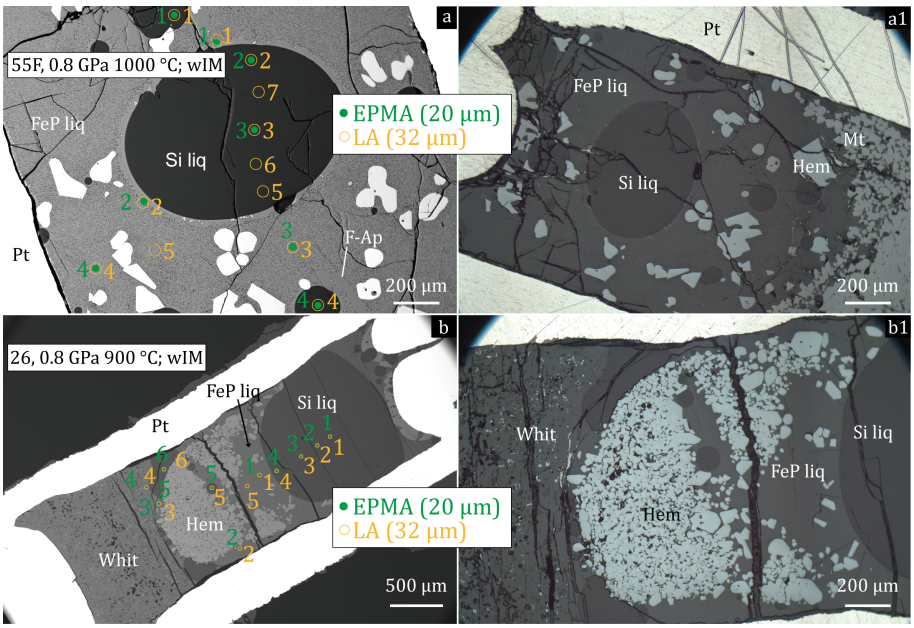

Figure S-5 Examples of analytical locations, shown by **(a–a1)** run 55F and **(b–b1)** run 26, that contain different melt pools. Abbreviations same as Figure S-4. Left panels are BSE images, and right panels are optical reflected light photographs.

5. Trace Element Analyses

Except for runs 57F and 58F, which contain liquid pools too small to measure, all runs were measured for trace elements in quenched melts. Run 20 has FeP liquids with two different kinds of impurities (*e.g.*, Si liquid droplets and unidentified Fe-rich droplets; Fig. S-4c1) and Si-rich liquids with many tiny impurities (*e.g.*, quartz and FeP droplets; Fig. S-4c2),

making trace element data inconsistent between repeat analyses, hence run 20 was not used for partition coefficient (*D*) calculation. For each quenched melt, three to eight points were measured (Fig. S-5). Trace element abundances of the immiscible FeP- and Si-rich melts were determined by laser ablation-inductively coupled plasma-mass spectrometry (LA-ICP-MS) employing an Element XR HR-ICP-MS instrument (Thermo Fisher Scientific, USA) coupled to an Analyte G2 193 nm ArF excimer laser ablation system at the State Key Laboratory of Lithospheric and Environmental Coevolution, IGGCAS. The approach is similar to that outlined in Wu *et al.*, (2018a) with isotopes measured using a peak-hopping mode with a laser diameter of ~32 μm and 3 Hz repetition rate. For run 22, the diameter is of ~16 μm with a 5 Hz repetition rate. The laser energy density is ~4.0 J/cm^2. The Element XR is equipped with a jet-interface, comprising of a jet sample cone, an X-version skimmer cone and a high-capacity vacuum pump (OnTool Booster 150, Asslar, Germany). This leads to a signal enhancement in laser sampling mode by a factor of 3–5, resulting in an improved detection capability. Helium was employed as the ablation gas to improve the transporting efficiency of ablated aerosols. NIST SRM 610 reference glass was used for external calibration and ARM-1 (Wu *et al.*, 2019) and OJY-1 glass were used for quality control monitoring. Calcium (^{43}Ca) was used as an internal standard. The resulting data were reduced using the Iolite program with the bulk normalisation as 100 % (m/m) (Wu *et al.*, 2018b). In the few cases where deeply buried impurities were encountered, their presence was identified in the time-resolved signal and readily removed before data processing. For most trace elements (>0.005 μg/g), the accuracy is better than ±10 % with analytical precision (1 RSD) of ±10 %. Occasionally, negative values or values of 2 RSD above 100 % are below the detection limit and not used (*e.g.*, Fig. 3).

Table S-2 Summary of melt major elements based on average compositions for each experiment.

	SiO_2	Al_2O_3	P_2O_5	FeOt	MgO	CaO	Na_2O	TiO_2	K_2O	F'	MnO	Total*
nIM Si liq	55.0–55.9	10.4–10.8	5.5–6.3	15.3–15.9	0.8–1.0	4.7–5.0	4.9–5.8	0.4–0.6	0.06–0.14		0.4–0.6	99.0–100.6
nIM FeP liq	28.5–31.9	5.8–6.5	16.7–19.6	26.5–27.1	1.9–2.1	10.8–11.9	3.1–3.6	0.8–0.9	0.02–0.05		1.0–1.1	100.5–100.6
mIM Si liq	54.5–63.6	8.1–10.3	2.2–7.4	4.3–13.2	0.3–0.8	0.8–4.8	4.1–5.6	0.2–0.5	0.04–0.09		0.2–0.4	92.3–94.0
mIM FeP liq	13.6–26.3	3.9–5.3	21.4–33.0	21.2–29.1	1.9–4.2	10.8–17.5	3.0–3.4	0.3–1.2	0.02–0.04		0.9–1.8	94.6–98.6
wIM Si liq	63.6–74.9	10.2–13.7	1.2–4.1	1.5–4.8	0.1–0.4	0.1–0.8	4.9–6.6	0.04–0.4	0.05–0.08	0.6	0.07–0.19	89.0–99.3
wIM FeP liq	2.3–7.0	0.4–7.9	36.3–43.1	17.0–34.9	4.7–9.7	4.0–13.7	2.9–5.8	0.08–0.9	0.01–0.04	0.9–3.2	2.0–3.5	94.3–101.7

' Only show F concentrations of 53F, 57F, and 58F, as their liquids contain minimal impurities.
* Totals below 100 wt. % mainly due to nm–μm epoxy bubbles and H_2O in the resultant glass (*e.g.*, Fig. 2e).

6. Geochemical Characteristics

Major elements of all synthesised liquids and FeP crystals are shown in Figures 1, 3 and Table S-2, with detailed data present in Dataset S-1. Trace elements and *D* values of 11 runs (Fig. 3d) are summarised in Dataset S-2, and the point-by-point data are listed in Datasets S-3 to S-12.

7. Equilibrium of Experiments

Figure S-6 shows that three representative runs of different immiscible degree all have consistent major and trace element concentrations, showing the equilibrium between two immiscible melts. Although the Ce(max/min) of silicate liquids from 56 and 47F—used as a proxy for the REE—show variation from 1.5–1.9 (Table 1), their elements are generally consistent (Fig. S-7), hence their immiscible melts are still thought to be well equilibrated. Relationship between temperature and $D^{LFeP–LSi}$ values further demonstrates adequate chemical exchange and equilibrium between the resultant immiscible FeP and silicate liquids in our experiments (Fig. S-8). Elemental variations of runs 53F, 54F, and 59F, deriving their complex "semi equilibrated" status, were shown in Figures S-9 and S-10.

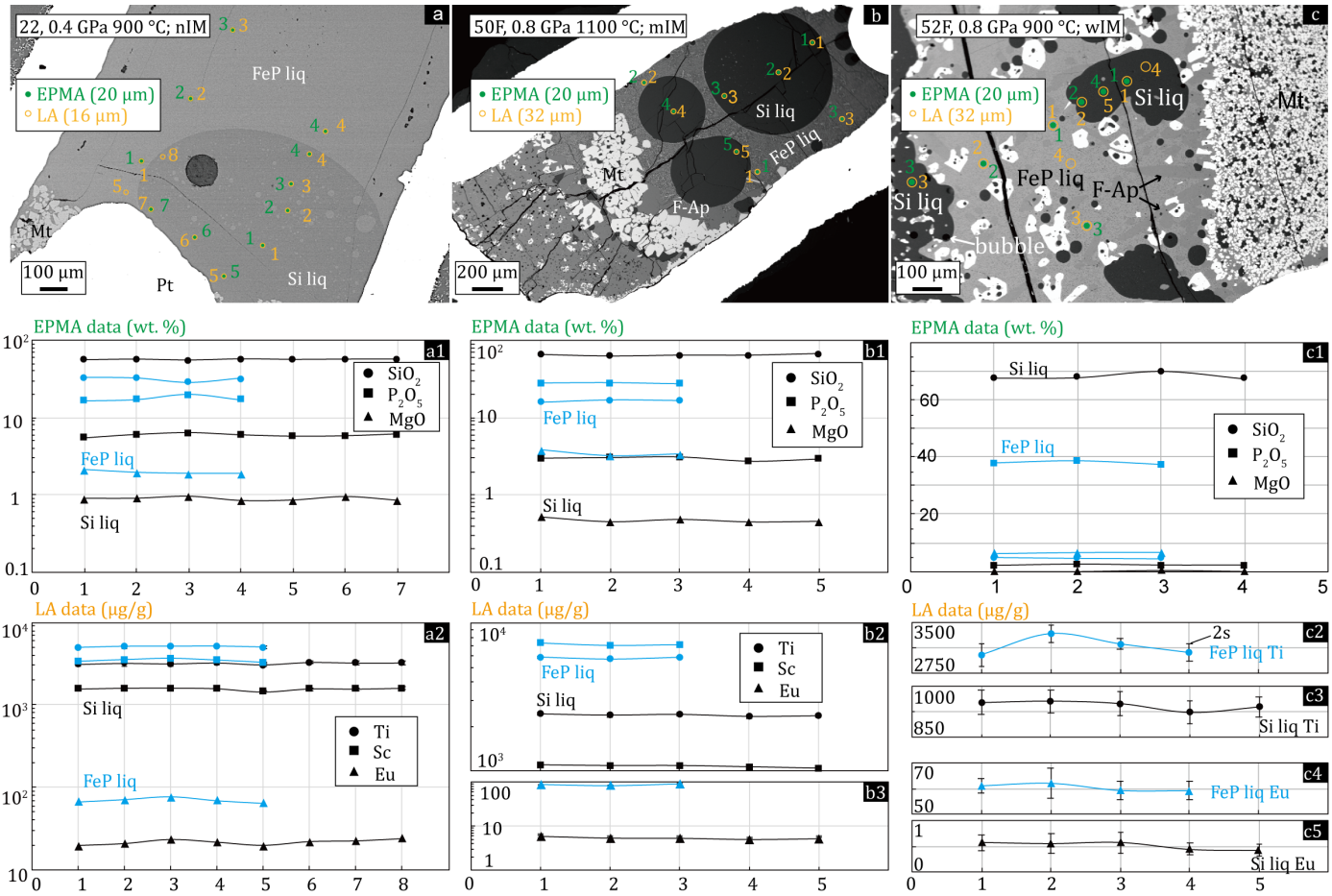

Figure S-6 Consistent major and trace element contents from runs of different immiscibility degree showing the equilibrium between two melts. **(a–a2)** run 22; **(b–b3)** run 50F; **(c–c5)** run 52F. Abbreviations are as in Figure S-4.

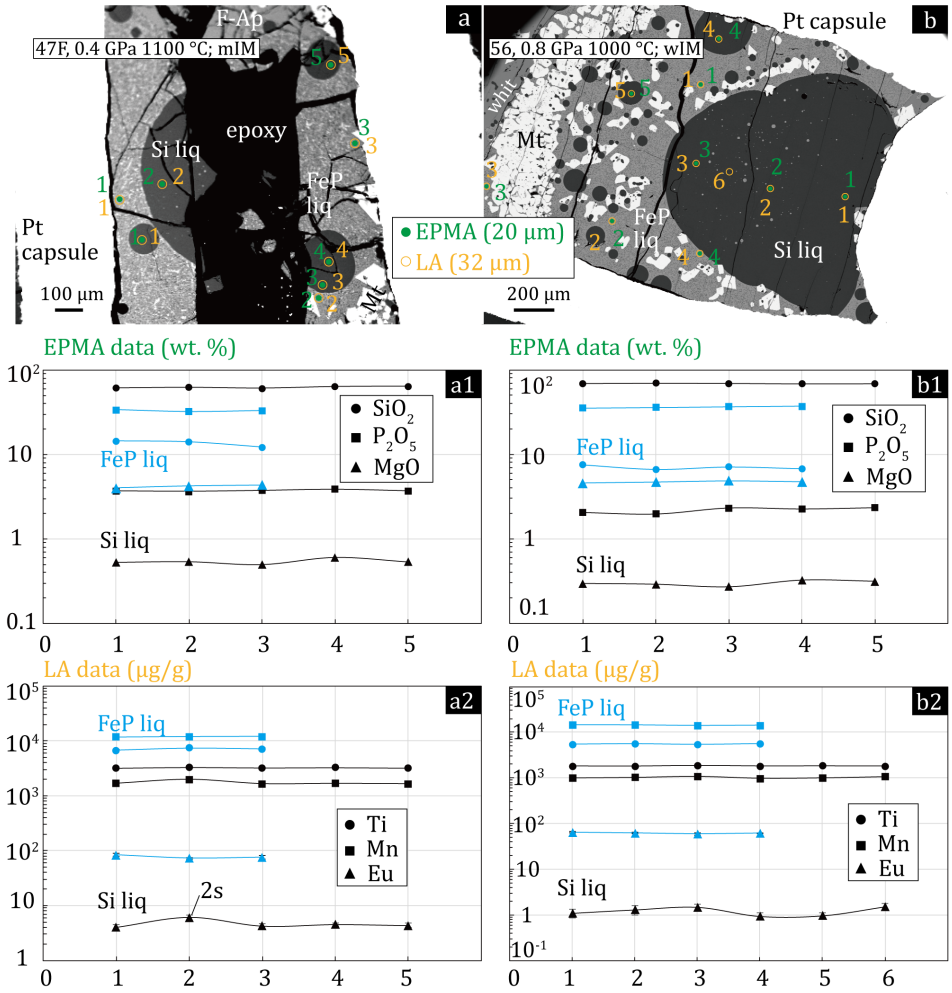

Figure S-7 General consistent element contents of **(a–a2)** run 47F and **(b–b2)** run 56. Abbreviations same as Figure S-4.

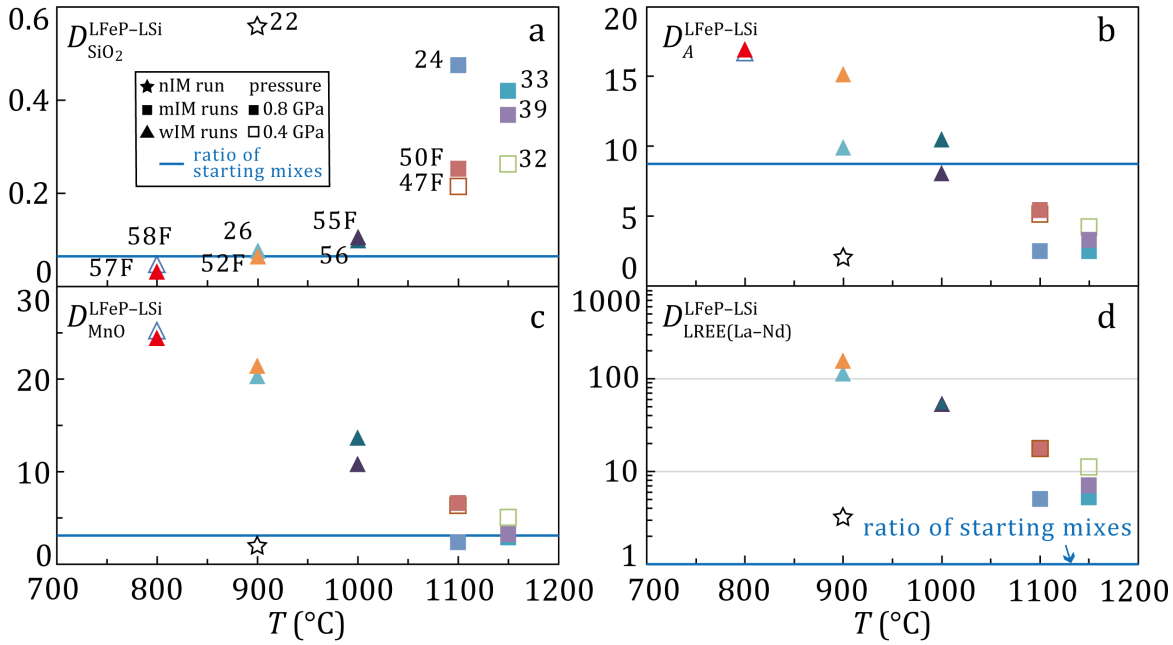

Figure S-8 $D^{\text{LFeP–LSi}}$ values *versus* temperature, showing immiscible liquids of wIM and mIM runs have compositions different from starting compositions and their $D^{\text{LFeP–LSi}}$ values are temperature dependent, supporting adequate chemical exchange and equilibrium between the resultant FeP and silicate liquids. In **(b)**, $A = TiO_2 + FeO_{total} + MgO + CaO + P_2O_5$ (wt. %). Runs 57F and 58F are plotted for comparison.

For runs 53F, both 16 μm spot and 32 μm spot LA data were plotted for reference. *D* values of runs 53F, 54F, and 59F are not discussed due to the half-equilibrium status. In detail, for wIM runs 53F, 54F, and 59F, we found consistent elemental compositions for FeP liquids (Figs. S-9, S-10). For the Si liquids, elements such as Mn, Rb, Sr, Li, Mg, K, Fe, Co, Cu, Zn, Ge, Ag, Cs, Ba, Pb were consistent across spatially separated analyses and therefore considered to be equilibrated with FeP liquids. Trace elements such as the REE also demonstrate relatively good equilibrium. For example, Ce concentrations were mostly consistent for Si liquids. The worst-case scenario is in experiment 53F where Ce contents of silicate droplets varied from 1.16 to 6.33 μg/g (factor of 5.5) between different analytical spots within the same phase (Table 1). This difference is negligible relative to the Ce ratios between FeP and silicate liquids (Fig. 3e), and inter-experiment variability. Some elements in Si liquids (*e.g.,* Ti, Nb, Ta) exhibited substantial variability for runs 53F, 54F, and 59F (Figs. S-9, S-10). Considering this semi-equilibrium condition, *D* values of these three runs are excluded from discussion. Runs 57F and 58F yielded dendritic magnetite, indicating that the Fe-oxide liquids are depolymerised and crystallise during quench. Liquids of runs 20, 57F and 58F are too small for LA analyses, hence demonstration of elemental consistency is challenging, and *D* values are not discussed.

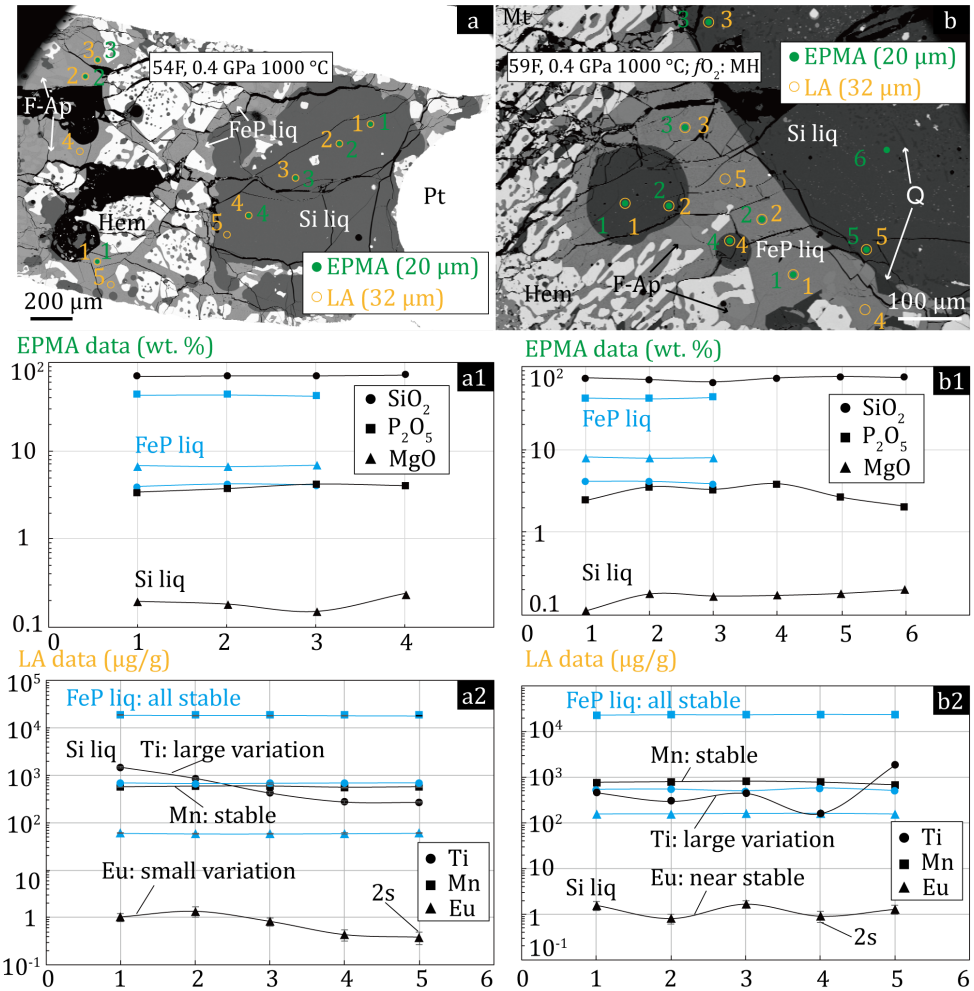

Figure S-9 Elemental variations of **(a–a2)** run 54F and **(b–b2)** 59F. Major elements are generally consistent, while trace elements show either consistent, large, or small variations. Abbreviations same as Figure S-4.

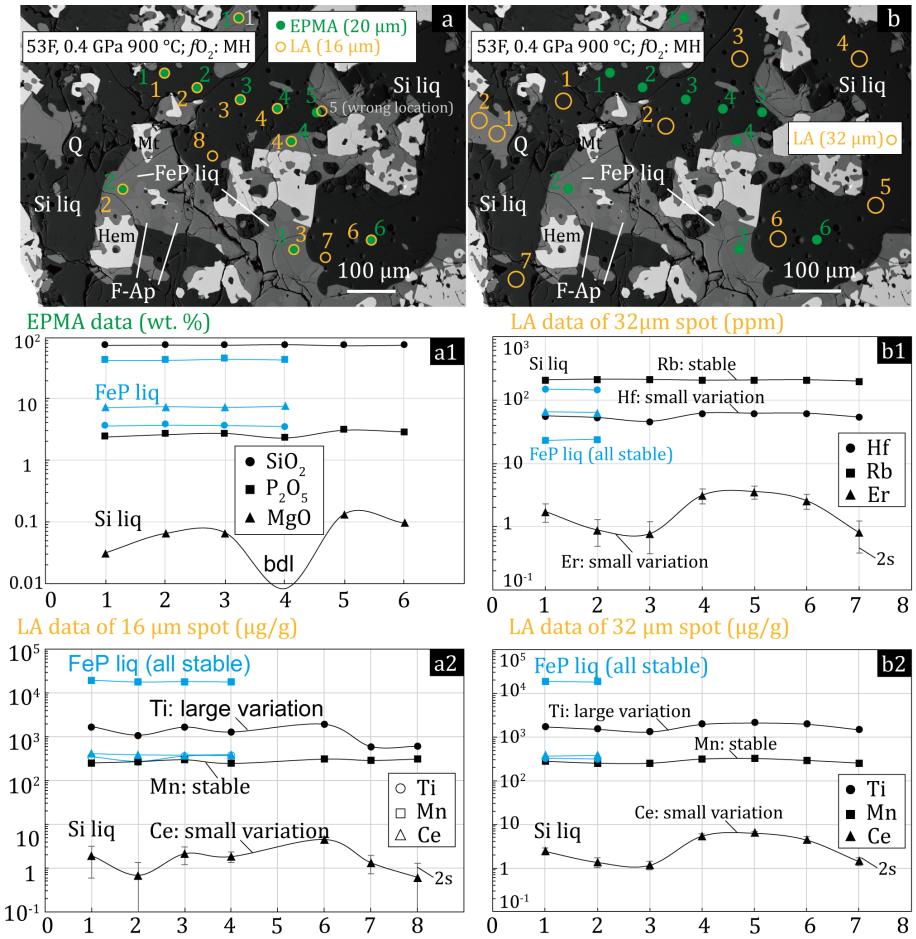

Figure S-10 Elemental variations of run 53F. Major elements are generally consistent, while trace elements show either consistent, large, or small variation for both **(a–a2)** 16 µm and **(b–b2)** 32 µm spots. Abbreviations same as Figure S-4.

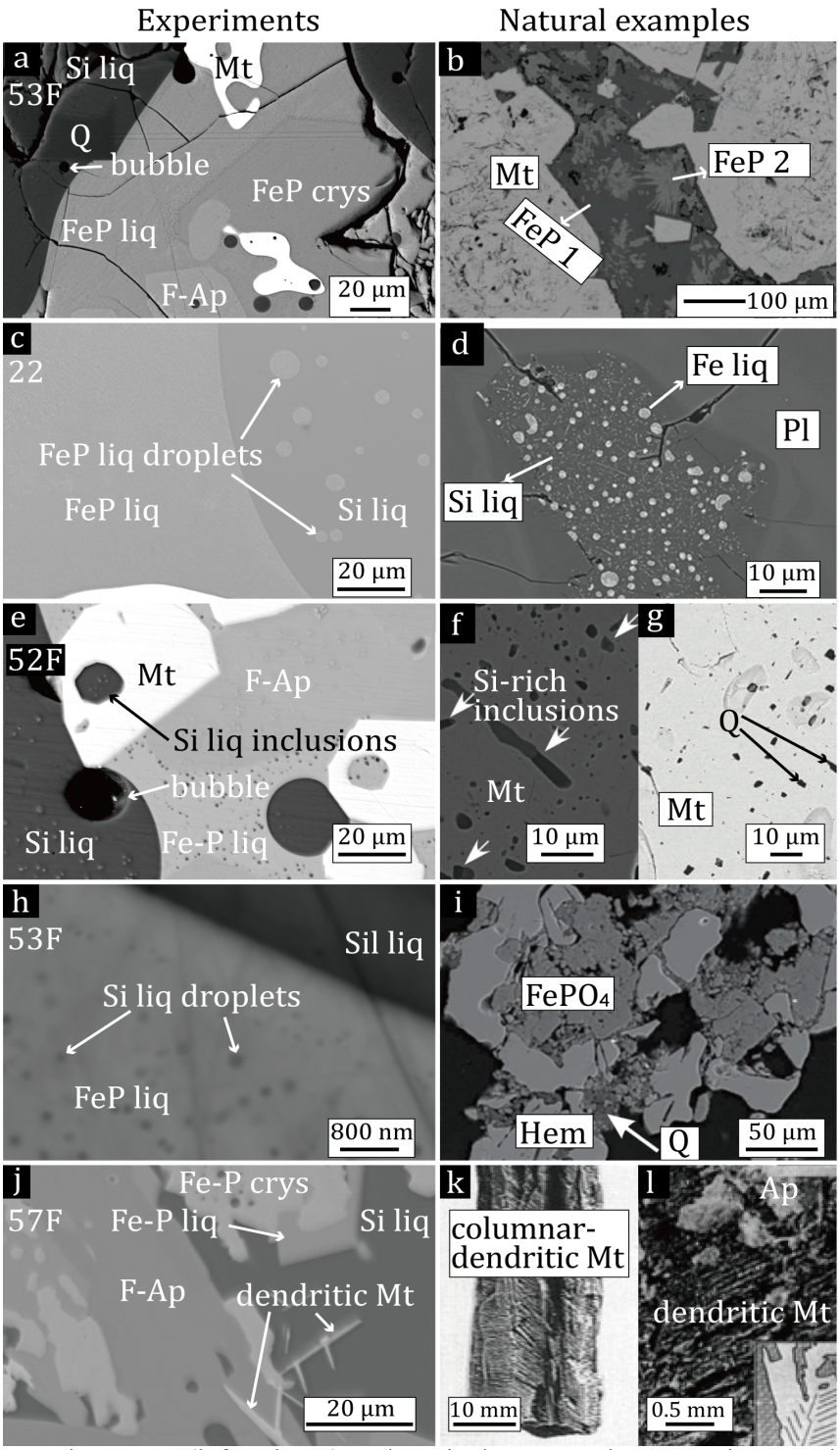

Figure S-11 Experimental textures (left column) and equivalent natural textures in IOA deposits (right column), shown by **(a, b)** two FeP phases, **(c, d)** FeP liq droplets surrounded by Si liquids, **(e–g)** Si-rich inclusions or quartz inside magnetite, **(h, i)** Si liquid droplets or quartz in FeP phases, and **(j–l)** dendritic magnetite. References: **(b)** El Laco (Xie *et al.*, 2019); **(d)** El Laco (Velasco *et al.*, 2016); **(f)** El Laco (Tornos *et al.*, 2024); **(g)** El Romeral (Rojas *et al.*, 2018); **(i)** El Laco (Mungall *et al.*, 2018); **(k)** El Laco (Nyström and Henríquez, 1994); **(l)** Kiruna (Nyström and Henriquez, 1989). Abbreviations: Pl, plagioclase; others same as Figure S-4.

Supplementary Datasets

Dataset S-1 Major elements of glasses.
Dataset S-2 Trace elements of glasses and *D* values.
Dataset S-3 Trace elements of Run 22_ARM-1 (16 µm).
Dataset S-4 Trace elements of Run 39_ARM-1.
Dataset S-5 Trace elements of Runs 26 52F_ARM-1.
Dataset S-6 Trace elements of Runs 32 33_ARM-1.
Dataset S-7 Trace elements of Runs 50F 24_ARM-1.
Dataset S-8 Trace elements of Runs 56 47F_ARM-1.
Dataset S-9 Trace elements of Runs 59F 55F_ARM-1.
Dataset S-10 Trace elements of Runs 20 54F_ARM-1.
Dataset S-11 Trace elements of Run 53F_ARM-1 (16 µm; for reference only).
Dataset S-12 Trace elements of Run 53F_ARM-1 (32 µm; for reference only).

Datasets S-1 and S-2 (.xlsx) and S-3 to S-12 (.xlsx files in a single .zip directory) are available for download (.xlsx) from the online version of this article at http://doi.org/10.7185/geochemlet.2436.

Supplementary Information References

Charlier, B., Namur, O., Toplis, M.J., Schiano, P., Cluzel, N., *et al.* (2011) Large-scale silicate liquid immiscibility during differentiation of tholeiitic basalt to granite and the origin of the Daly gap. *Geology* 39, 907–910. https://doi.org/10.1130/g32091.1

Fischer, L.A., Wang, M., Charlier, B., Namur, O., Roberts, R.J., *et al.* (2016) Immiscible iron- and silica-rich liquids in the Upper Zone of the Bushveld Complex. *Earth and Planetary Science Letters* 443, 108–117. https://doi.org/10.1016/j.epsl.2016.03.016

Hou, T., Charlier, B., Holtz, F., Veksler, I., Zhang, Z., *et al.* (2018) Immiscible hydrous Fe–Ca–P melt and the origin of iron oxide-apatite ore deposits. *Nature Communications* 9, 1415. https://doi.org/10.1038/s41467-018-03761-4

Kamenetsky, V.S., Charlier, B., Zhitova, L., Sharygin, V., Davidson, P., Feig, S. (2013) Magma chamber-scale liquid immiscibility in the Siberian Traps represented by melt pools in native iron. *Geology* 41, 1091–1094. https://doi.org/10.1130/g34638.1

Lester, G.W., Clark, A.H., Kyser, T.K., Naslund, H.R. (2013) Experiments on liquid immiscibility in silicate melts with H_2O, P, S, F and Cl: implications for natural magmas. *Contributions to Mineralogy and Petrology* 166, 329–349. https://doi.org/10.1007/s00410-013-0878-1

Lledo, H.L., Naslund, H.R., Jenkins, D.M. (2020) Experiments on phosphate–silicate liquid immiscibility with potential links to iron oxide apatite and nelsonite deposits. *Contributions to Mineralogy and Petrology* 175, 111. https://doi.org/10.1007/s00410-020-01751-8

Mungall, J.E., Long, K., Brenan, J.M., Smythe, D., Naslund, H.R. (2018) Immiscible shoshonitic and Fe-P-oxide melts preserved in unconsolidated tephra at El Laco volcano, Chile. *Geology* 46, 255–258. https://doi.org/10.1130/g39707.1

Nyström, J.O., Henriquez, F. (1989) Dendritic magnetite and miniature diapir-like concentrations of apatite: Two magmatic features of the Kiirunavaara iron ore. *GFF* 111, 53–64. https://doi.org/10.1080/11035898909454759

Nyström, J.O., Henriquez, F. (1994) Magmatic features of iron ores of the Kiruna type in Chile and Sweden; ore textures and magnetite geochemistry. *Economic Geology* 89, 820–839. https://doi.org/10.2113/gsecongeo.89.4.820

Rojas, P.A., Barra, F., Deditius, A., Reich, M., Simon, A., *et al.* (2018) New contributions to the understanding of Kiruna-type iron oxide-apatite deposits revealed by magnetite ore and gangue mineral geochemistry at the El Romeral deposit, Chile. *Ore Geology Reviews* 93, 413–435. https://doi.org/10.1016/j.oregeorev.2018.01.003

Tornos, F., Hanchar, J.M., Steele-MacInnis, M., Crespo, E., Kamenetsky, V.S., Casquet, C. (2024) Formation of magnetite-(apatite) systems by crystallizing ultrabasic iron-rich melts and slag separation. *Mineralium Deposita* 59, 189–225. https://doi.org/10.1007/s00126-023-01203-w

Veksler, I.V., Charlier, B. (2015) Silicate Liquid Immiscibility in Layered Intrusions. In: Charlier, B., Namur, O., Latypov, R., Tegner, C. (Eds.) *Layered Intrusions*. Springer, Dordrecht, 229–258. https://doi.org/10.1007/978-94-017-9652-1_5

Velasco, F., Tornos, F., Hanchar, J.M. (2016) Immiscible iron- and silica-rich melts and magnetite geochemistry at the El Laco volcano (northern Chile): Evidence for a magmatic origin for the magnetite deposits. *Ore Geology Reviews* 79, 346–366. https://doi.org/10.1016/j.oregeorev.2016.06.007

Wu, S., Karius, V., Schmidt, B.C., Simon, K., Wörner, G. (2018a) Comparison of Ultrafine Powder Pellet and Flux-free Fusion Glass for Bulk Analysis of Granitoids by Laser Ablation-Inductively Coupled Plasma-Mass Spectrometry. *Geostandards and Geoanalytical Research* 42, 575–591. https://doi.org/10.1111/ggr.12230

Wu, S.-T., Huang, C., Xie, L.-W., Yang, Y.-H., Yang, J.-H. (2018b) Iolite Based Bulk Normalization as 100% (*m*/*m*) Quantification Strategy for Reduction of Laser Ablation-Inductively Coupled Plasma-Mass Spectrometry Transient Signal. *Chinese Journal of Analytical Chemistry* 46, 1628–1636. https://doi.org/10.1016/s1872-2040(18)61118-1

Wu, S., Wörner, G., Jochum, K.P., Stoll, B., Simon, K., Kronz, A. (2019) The Preparation and Preliminary Characterisation of Three Synthetic Andesite Reference Glass Materials (ARM-1, ARM-2, ARM-3) for *In Situ* Microanalysis. *Geostandards and Geoanalytical Research* 43, 567–584. https://doi.org/10.1111/ggr.12301

Xie, Q., Zhang, Z., Hou, T., Cheng, Z., Campos, E., *et al.* (2019) New Insights for the Formation of Kiruna-Type Iron Deposits by Immiscible Hydrous Fe-P Melt and High-Temperature Hydrothermal Processes: Evidence from El Laco Deposit. *Economic Geology* 114, 35–46. https://doi.org/10.5382/econgeo.2019.4618

Yokoo, S., Hirose, K., Tagawa, S., Morard, G., Ohishi, Y. (2022) Stratification in planetary cores by liquid immiscibility in Fe-S-H. *Nature Communications* 13, 644. https://doi.org/10.1038/s41467-022-28274-z